Technical University of Denmark

DTU

Effect of Infiltration Material on a LSM15/CGO10 Electrochemical Reactor in the Electrochemical Oxidation of Propene

Ippolito, Davide; Kammer Hansen, Kent

Link back to DTU Orbit

DTU Library
Technical Information Center of Denmark

Effect of Infiltration Material on a LSM_{15}/CGO_{10} Electrochemical Reactor in the Electrochemical Oxidation of Propene

Davide Ippolito[a], Kent Kammer Hansen[a]

[a] Department of Energy Conversion and Storage, Technical University of Denmark, Frederiksborgvej 399, 4000, Roskilde

Phone: +45 46775602, Fax +45 46775858, e-mail address: davi@dtu.dk

Abstract

The effect of infiltrating on a $La_{0.85}Sr_{0.15}MnO_3$/$Ce_{0.9}Gd_{0.1}O_{1.95}$ 11-layer electrochemical reactor with CeO_2 and $Ce_{0.8}Pr_{0.2}O_{2-\delta}$ was studied in propene oxidation at open circuit voltage and under polarization as a function of reaction temperature. This work outlined the importance of catalytic and electrochemical properties of infiltrated material on the ability to increase propene conversion under polarization with good faradaic efficiency. Electrochemical impedance spectroscopy (EIS) was used to study the effect of infiltration material on electrode properties. The infiltration of a mixed ionic and electronic conductor (MIEC), like $Ce_{0.8}Pr_{0.2}O_{2-\delta}$, increased the electrode performance at low temperature but decreased the lifetime of the oxygen ion promoters on the catalyst/electrode surface, reducing the faradaic efficiency of the reaction. The infiltration of CeO_2 provided high propene conversion at open circuit and high effect of polarization associated with good faradaic efficiency, especially at low temperature.

1

Introduction

Air pollution from stationary and mobile sources has become one of most important environmental concerns of the last ten years. Stricter legislation on emission control has been adopted in the US, Europe and also emerging countries, like India and China [1]. Exhaust gases from spark and compression engines contribute to the degradation of air quality, especially in urban environments. Between these two, Diesel exhausts contain high levels of NO_X, volatile organic compounds (VOC) and fine particulate matter (PM) contributing to respiratory problems and cardiovascular disease [2,3]. Supported metal catalysts, such as Pt and Pd, are usually employed both for catalytic combustion of hydrocarbons and NOX reduction [4]. They are very active at low temperature but suffer from high temperature sintering, poisoning from sulphur and their use is limited by high prices. Alternative catalysts have thus been explored, such as hexaaluminates, single and doped transition metal oxides and perovskite [5].

Transition metal perovskites ($LaMO_3$) (M=Mn,Co) are possible alternative catalysts to noble metals in hydrocarbon combustion reactions due to the redox properties of the M cation, the presence of lattice defects and weakly bonded oxygen at the surface. They offer good thermal stability in oxygen and steam-rich atmospheres and low cost, but they currently have lower efficiencies [6,7]. For example, Spinicci et al. studied the

2

activity of LaMnO$_3$ and LaCoO$_3$ towards combustion of VOCs and oxygen surface species mobility was identified as a requisite for high catalytic activity [8].

Catalyst activity can be enhanced by using Electrochemical Promotion of Catalysis (EPOC). EPOC is based on the control of catalyst work function by applying a potential or current to an electrocatalyst interfaced with a solid electrolyte. In 1981, for example, Stoukides and Vayenas [9] demonstrated increased reaction rate and selectivity in ethylene catalytic oxidation on Ag. This phenomenon has also been studied using perovskite as a catalyst; Gaillard et al. demonstrated *in situ* control of activity and selectivity of La$_{0.8}$Sr$_{0.2}$Co$_{0.8}$Fe$_{0.2}$O$_3$ for deep oxidation of propene at 450 °C in air by EPOC [10]. Additionally, Roche et al. presented an electrochemical promotion effect for the deep oxidation of propane on lanthanum manganite [11]. Furthermore, Tsiakaras et al. studied the electrocatalytic behaviour of La$_{0.6}$Sr$_{0.4}$Co$_{0.8}$Fe$_{0.2}$O$_3$ perovskite deposited on yttria-stabilized zirconia (YSZ) during methane oxidation where oxygen was electrochemically supplied as O^{2-} and found considerable changes in methane conversion and product selectivity [12]. Finally, Balomenou et al. developed a monolith electrochemical plate reactor (MEPR) using Pt and Rh dispersed on a YSZ plate to measure the abatement of simulated and real automotive pollution and achieved electrochemical promotion in both situations [13].

The present work studied the possibility of using an 11-layer porous single chamber electrochemical reactor for the oxidation of propene, a major Diesel exhaust emission component [14], without precious metal. In this work, the whole reactor was thought of as a catalytic filter with a porous composite electrode interfaced with a porous

electrolyte for Diesel exhaust after-treatment. Ceria is one of the best hydrocarbon oxidation catalysts known, and although ceria-based oxidation catalysts are normally coupled with a precious metal, alumina-supported ceria shows sufficient activity in the oxidation of unburned hydrocarbons in Diesel exhausts without the addition of precious metals [15]. In order to enhance the catalytic activity for a future full-scale application, the effect of CeO_2 and $Ce_{0.8}Pr_{0.2}O_{2-\delta}$ impregnation on reactor activity was therefore investigated. The influence of infiltrated material properties on the reactor performance was also investigated. To comply with these objectives, electrochemical impedance spectroscopy (EIS) was employed.

Experimental

Cell preparation

The 11-layer electrochemical reactor (backbone) was prepared by laminating layers of electrode and electrolyte made by tape casting for a total of 5 single cells. The electrolyte tape was made of $Ce_{0.9}Gd_{0.1}O_{1.95}$ purchased from Rhodia, while the electrode was made of a 35% weight $Ce_{0.9}Gd_{0.1}O_{1.95}$ (CGO_{10}) and 65% weight $La_{0.85}Sr_{0.15}MnO_3$ (LSM_{15}) composite (Haldor Topsoe). Slurries for tape casting were made from metal oxide powder, solvent, binder and carbon as pore former. The slurries were ball milled before tape casting. The cell was then sintered at 1250 °C for 2 h. The average diameter of the cells was 13 mm.

The cells were impregnated using a 1.5 M solution of 20 mol% $Pr(NO_3)_3$ + 80 mol% $Ce(NO_3)_3$ for $Ce_{0.8}Pr_{0.2}O_{2-\delta}$ (CPO_{20}) infiltration and with a 1.5 M solution of $Ce(NO_3)_3$ for CeO_2 infiltration with Triton X-100 as surfactant. Solutions were prepared with Millipore water, Triton X-100 (Sigma-Aldrich), Ce nitrate hexahydrate (Alfa Aesar) and Pr nitrate hydrate (Alfa Aesar). Infiltration was carried out in one step by applying vacuum to the cell after application of impregnation solution. After infiltration, the cell was calcined at 600 °C for 2 h. The weight of the cell was measured before infiltration and after calcination to estimate the infiltration loading. The infiltration loading was equivalent to approximately 2.6-2.7% of the weight of the cell. Gold paste with 20% weight carbon was painted on both sides of the electrochemical reactor and used as the current collector. The cell weights were measured without the current collector and the cell areas were approximately 1.429 and 1.409 cm^2 for CPO_{20} and CeO_2 infiltrated cells, respectively.

5

Reactor configuration

Figure 1 illustrates the reactor configuration. The sample was mounted in a tubular reactor between two alumina tubes with contact between the gold paste and the two Pt electrodes used as working and reference/counter electrodes under one atmosphere, as reported by Werchmeister et al. [16]. The setup was placed inside a glass tube surrounded by a furnace. For the catalytic activity evaluation, a mixture of 10% O_2 (Air Liquide; 20% O_2 ± 2% Ar), 1000 ppm propene (Air Liquide; 1% ± 0.02% propene in Ar) and Ar to balance was used with a total flow rate of 2 L h^{-1} controlled by Brooks flow meters. Reactants and products were analysed by an on-line Agilent 6890 N gas chromatograph connected to the reactor and equipped with Hayesep N and Molsieve columns and a thermal conductivity detector. The reaction temperature was monitored by two thermocouples: one touching the cell and the other one placed 4 mm over the cell. The temperature range of the measurements was 300 °C - 500 °C.

6

Cell structural characterization

The 11-layer reactor morphology and infiltrated particle morphology were characterised with a Zeiss Supra-35 scanning electron microscopy (SEM). In addition, adsorption/desorption experiments (BET) using Krypton were conducted on the infiltrated samples to determine the specific surface area (SSA). The samples were measured in an Autosorp-1-MP before and after catalytic measurements where all the samples were de-gassed for 3 h under vacuum at 300 °C prior to adsorption. The BET specific surface areas were calculated from the adsorption isotherm keeping the values of the relative Krypton pressure (p/p_0) between 0.05 and 0.3 for all samples. Finally, X-ray diffraction (XRD) measurements were carried out with a STOE theta-theta diffractometer using Cu Kα (λ=1.540 Å) from 20° to 100° and with a 0.05 2θ step size.

Cell activity characterization

The polarisation effect on the cell is characterised by the rate enhancement ratio (ρ) defined by:

$$\rho = \frac{r}{r_0}$$

where r_0 is the catalytic rate (mol/s) at open circuit voltage (OCV) and r is the catalytic rate (mol/s) under polarization

The faradaic efficiency was thus calculated as:

$$\Lambda = \frac{r - r_0}{\dfrac{I}{F}}$$

7

where *I* is the current and *F* is Faraday´s constant.

Cell electrochemical characterization

A potentiostat (Gamry, reference 600 USA) was used to perform chronoamperometry tests and for recording impedance spectra. The open-circuit voltage of the cell was stabilised before every measurement. The impedance spectra were recorded at open-circuit voltage (OCV) and with an anodic bias of +4 V (+ 800 mV/cell) with respect to the open circuit voltage with an amplitude of 36 mV RMS over the frequency range 0.78 MHz to 5 mHz with 10 points/decade. The chronoamperometry tests were carried out for 2 h with anodic potentials from +200 mV/cell to 1 V/cell with respect to the open-circuit voltage with 1 V steps followed by cathodic polarisation using the same procedure. The ohmic drop was not subtracted in the given potentials. The temperature range of these measurements was 300 °C - 500 °C.

The impedance spectra were analysed in ZSimpWin 3.21 software using Complex Non-Linear Square (CNLS) fitting. The inductance coming from the wiring was subtracted for every spectrum to perform the fitting. The spectra were validated using the Kramers-Kronig test for causality and time invariance.

An equivalent circuit was used containing a serial resistance, Rs, and a number of RQ or RG subcircuits. RQ is a resistance R in parallel with a Constant Phase Element (CPE). The impedance of a CPE is given by:

$$\frac{1}{Z} = Y = Y^o(j\omega)^n$$

where Z is the impedance, Y the admittance, Y^0 is the amplitude of the constant phase element admittance, j is the imaginary number and ω is the frequency.

The general impedance of the Gerischer element (G) is expressed by:

$$Z_G = \frac{1}{Y_o\sqrt{K_A + i\omega}}$$

where Y_0 is the admittance parameter and K_A is the rate constant parameter.

The distribution of relaxation times (DRT) analysis was performed using in-house software based on Schichlein et al. [17]. The visual Hanning filter was used for data filtering and the filtering values was kept fixed for all analyses.

Result and Discussion

Catalyst characterization

Figures 2 and 3 show the micrographs of CeO_2 and CPO_{20} infiltrated cells, respectively. The good coverage of CeO_2 and CPO_{20} particles on the LSM_{15}-CGO_{10} surfaces was noticeable; the particles were arranged along the walls of the pores without blocking them. The formation of solid solution between Ce and Pr was guaranteed by the exothermicity of Triton X-100 decomposition. Moreover, the XRD recorded on CPO_{20} powder and visible in Figure 4 displays nearly all of the characteristic reflections corresponding to the fluorite structure of CeO_2. No crystalline phases except the fluorite-type solid solution were detected, suggesting direct solid solution formation.

The CPO_{20} particles showed different agglomeration behaviour with respect to CeO_2, one that has already been reported by Kharton et al. [18], where a $Ce_{0.8}Gd_{0.18}Pr_{0.02}O_{2-\delta}$ composite showed segregated Pr and Gd enriched particles along the grain boundaries. Co-doping with Pr increased the tendency for phase segregation along the grain boundaries of $Ce(Gd)O_{2-\delta}$. Also in this case, the introduction of Pr^{+4} ions could have changed the nucleation properties of CeO_2 on the LSM_{15}/CGO_{10} composite backbone, giving rise to a diffusion of Pr ions into LSM_{15} and CGO_{10}. However, the formation of perovskite phases like $PrMnO_3$ could not be excluded.

CeO_2 was found to have a specific area of 2.43 m^2/g. CeO_2 area is higher than the one of CPO_{20} which is equal to 1.64 m^2/g. This is due to the different particle morphologies. From the SEM micrographs it was possible to observe that the distribution of CeO_2 particles was more uniform and the adhesion of CeO_2 on the backbone surface was

more optimal than CPO_{20}. Additionally, the infiltration procedure was able to increase the specific area of the backbone cell by at least one order of magnitude [19].

Catalyst activity tests

Figure 5 shows the intrinsic catalytic reaction rate towards propene oxidation measured at open circuit voltage (OCV). The CeO_2 infiltrated cell showed higher reaction rates with respect to the CPO_{20} infiltrated cell at all temperatures; the conversions of propene at 400 ºC for CeO_2 and CPO_{20} infiltrated cells were 46.8% and 37.7%, while at 300 ºC they were 17.8% and 13.5%, respectively. The better activity of CeO_2 at low temperature could be attributed only partially to the larger specific surface area. The selectivity towards CO_2 was almost 100% at all temperatures for CeO_2, but only 91-92% for the CPO_{20} infiltrated cell. Reddy et al. using XPS reported an enrichment of Pr in the surface region up to 44%, higher than that nominal content of 20% [26]. A partial surface segregation of Pr forming Pr_6O_{11} could be the reason for the lower activity of CPO_{20}. Pr_6O_{11} is recognised as a good catalyst for methane and CO oxidation due to its high redox potential, but the catalytic activity of praseodymia seems to be limited by the difficult reoxidation of Pr_2O_3 [20]. Pr_6O_{11} could have some activity for propene oxidation, but it could be relatively inactive compared to ceria due to the high stability of reduced Pr_2O_3. The lower selectivity to CO_2 observed for CPO_{20} with CO formation suggested that oxygen from Pr_6O_{11} was not utilised in the same way as from ceria under the reaction conditions. Zhao et al. observed a decrease in reaction rate for n-butane oxidation with the incorporation of Pr^{+4} into ceria. This decrease in reaction rate was

anyway lower than the reaction rate decrease observed for ceria doped with Sm, Gd, Nb and Ta [15]. As observed by Zhao et al. for the oxidation of n-butane over ceria and Samaria-doped ceria (SDC), the common assumption that doping ceria will increase its activity is not always correct [21]. If we compare the reaction rate of the backbone (3.88 10^{-8} mol C_3H_6/(s×g)) at 400 ºC as reported in [19], infiltration resulted in a substantial increase in reaction rate. The extraction of apparent activation energy was outside the scope of this analysis, and observing a slope change in the reaction rate curves due to possible diffusion limitations of reactants between 350 ºC and 400 ºC is difficult.

During the application of anodic polarization, being this reactor symmetric, one side worked as anode and the other side as a cathode. At the cathodic side molecular oxygen was reduced to lattice oxygen, which was then pumped by this anodic voltage through the oxygen vacancies of CGO_{10} to the surface of LSM_{15}. The pumped oxygen lattice on the anodic side can react directly with adsorbed propene to form CO_2 and H_2O or recombined to molecular oxygen through oxygen evolution reaction. Figure 6 shows the effect of polarisation at +4 V on the infiltrated cells at different reaction temperatures, expressed as rate enhancement ratio. It was possible to observe that the polarization effect was higher at low temperature for CeO_2 than for CPO_{20}, but it became more prominent on CPO_{20} with increasing temperature. The CeO_2 infiltrated cell reaction enhancement curve strongly flattened at temperatures higher than 400 °C possibly due to limiting reactant diffusion limitations inside the electrode pores; this phenomenon might limit the effect of polarization on propene conversion.

The rate enhancement ratio behaviour could be attributed to two types of regimes. Ceria has very low electronic and ionic conductivity, the latter being only 3% of the total

12

conductivity [22]. At low temperature (300-400 °C), some of the oxygen ions thus have the opportunity and time to backspillover from CGO_{10} on the deposited ceria surfaces and act as electronegative promoters of propene oxidation without recombine to form molecular oxygen. The increased propene reaction rate on CeO_2 at low temperatures could also be due to the contribution of a polarisation-induced double layer established between the O^{2-} back-spill on ceria surfaces and the O_2 adsorbed from the gas phase.

On the contrary, CPO_{20} has much higher electronic and ionic conductivity, behaving as a mixed ionic electronic conductor; the mixed conductivity was able to strongly expand the TPB area. This characteristic hindered the possible back-spill of oxygen ions to the CPO_{20} surfaces because the kinetics of promoter consumption, in the case of CPO_{20}, might be fast due to the high reactivity of the promoter at the three phase boundaries, as suggested by Roche et al. [11]. The O^{-2} recombination and following oxygen evolution, although the latter contributes to the total current, did not produce any increase in propene conversion. Figure 7 shows the behaviour of faradaic efficiency for CeO_2 and CPO_{20}. It is possible to observe that the two samples showed similar efficiency at high temperature (450-500 °C). Below this temperature range CPO_{20} exhibited a quasi-flat faradaic efficiency with decreasing temperature; CeO_2 instead showed a sharp increase with decreasing temperature. The explanation is given in the electrochemical characterization section.

13

Electrochemical characterization

Figures 8 and 9 show the Arrhenius plots of polarization resistance (R_p) at OCV and under polarisation for CPO_{20} and CeO_2 extracted from impedance spectra. CPO_{20} infiltration gave a better electrode performance, showing lower polarisation resistance at lower temperatures compared to CeO_2. This could be attributed to the mixed ionic-electronic conduction behaviour of CPO_{20}. CPO_{20} infiltration was also able to expand the TPB area and decrease the resistance associated with electrochemical reactions occurring on the surface. The activation energy of the R_p for CPO_{20} was 0.59 ± 0.03 eV, much lower than the activation energy of the CeO_2 infiltrated cell (0.97 ± 0.04 eV). This meant that the electrode performance for CPO_{20} was less susceptible to temperature decreases than for CeO_2. The activation energy of CeO_2 was close to the value of the backbone cell at OCV (0.93 ± 0.04 eV) reported in previous study [19]. The infiltration of CeO_2 was thus able to decrease the polarization resistance of the backbone without changing the reaction mechanism. Typical EPOC behaviour was visible in this case where a catalyst with high catalytic performance, like CeO_2/LSM_{15}, is coupled with an electrode with low exchange current at low temperature.

Figure 9 illustrates the Arrhenius plot of the polarization resistance measured at +4 V. At high temperatures (450-500 ºC) the decrease of R_p for CeO_2 upon anodic polarization was found to be very high, reaching resistance values similar to those obtained for CPO_{20}. Presumably the polarization response of the backbone became predominant on the infiltrated material polarization response. For this reason, at these temperatures, the faradaic efficiencies for both cells exhibited similar low values. At temperatures below 450 ºC, the effect of anodic polarization on CeO_2 polarization resistance drastically

14

decreased; high R_p coupled with good enhancement ratio (ρ) value caused the sharp increase of efficiency observed for CeO_2. For CPO_{20}, however, the effect of polarization decreased with much lower activation energy: low R_p coupled with low enhancement ratio (ρ) caused the flattening of the efficiency observed for CPO_{20}.The activation energy value extrapolated at high temperature for CPO_{20} curve was 0.82 ± 0.03 eV. The activation energy extracted for temperatures between 400 ºC and 300 ºC was 0.61 ± 0.01 eV instead; presumably the effect of mixed conductivity on R_p became predominant in this temperature range causing the slope change. The activation energy of polarization resistance (R_p) measured under polarization of +4 V for CeO_2 was 1.13 ± 0.05 eV; both the infiltrated exhibited an increase of activation energy under anodic voltage. This change of activation energy could be due to a modification of reaction mechanism establishing under polarization.

In order to obtain high faradaic efficiency it is necessary to reduce the speed of O^{2-} recombination to molecular oxygen and so to increase the promoter lifetime. In the case of CPO_{20} the kinetic of promoter consumption was very high (low R_p) also at low temperature if compared to CeO_2; this was the cause of low faradaic efficiency.

Figures 10 and 11 show the impedance spectra of CeO_2 and CPO_{20} infiltrated cells recorded at OCV and +4 V at 450 °C together with the Bode plot of the imaginary part of the recorded spectra. At least two depressed arcs were visible in these plots. The polarization to +4 V (0.8 mV/cell) strongly affected the impedance responses; a strong decrease in resistance was visible for the peak at low frequency for both infiltrated cells, as was an increase in characteristic peak frequency. Additionally, the impedance spectra under polarisation clearly displayed only two well defined depressed arcs where

15

the impedance contribution at medium frequency either disappeared or merged with the impedance response at low frequency. Moreover, the inclined line visible at medium frequency completely disappeared when polarisation was applied.

The impedance contribution at high frequencies (Figures 10c and 11c) was differently affected by polarization depending on the infiltration material. This impedance contribution at this temperature was likely due to oxygen ion transport from the electrolyte to the LSM_{15} electrode. The peak for the CeO_2 infiltrated cell was not affected by polarisation and the imaginary part of the spectra recorded under polarisation completely overlapped with the spectra recorded at OCV. On the contrary, the high frequency peak of the CPO_{20} infiltrated cell showed a small increase in resistance when polarised at +4 V associated with a peak frequency decrease. This meant that, in the case of CPO_{20}, it was possible to observe a charge transfer contribution even at these high frequencies; the overlapping between oxygen ion transport and electrode reactions could be due to the mixed conductivity of CPO_{20}.

The distribution of relaxation times (DRT) analysis visible in Figure 12 associated to the impedance spectra in oxygen and propene at 450 °C for CeO_2 and CPO_{20} showed three main peaks at high, medium and low frequencies. The peak at medium frequency was not well resolved and appeared as a shoulder overlapping the main peak at lower frequencies. The peak at high frequency (10.4 kHz) appeared at the same frequency and had similar resistance for both of the infiltration materials, so it was likely independent of infiltration material at high temperatures and at OCV. However, this effect could be attributed only to the backbone.

The reconstruction of CeO_2 impedance spectra through DRT analysis was only possible using three RQ elements, confirming the presence of a process at medium frequency. The DRT analysis for the CPO_{20} infiltrated cell showed behaviour typical of a Gerischer element at low frequency, as reported by Endler et al. with a single cell using a LSCF cathode [23]. The mixed ionic electronic behaviour of LSM_{15} usually visible at high cathodic polarization or low partial pressure of oxygen, associated to superficial oxygen vacancy formation, was enhanced by CPO_{20} infiltration. The Gerischer behaviour reflected that the overall oxygen reduction reaction on the mixed conducting CPO_{20} layers proceeded under the conditions where diffusion of oxygen vacancies in the electrode and diffusion of adsorbed oxygen species on electrode surface are kinetically coupled with the electrode exchange reaction between oxygen vacancies and gaseous oxygen (charge transfer reaction) at the electrode/gas interface [24].

Figure 13 and 14 exhibit the DRT analysis of the influence of reaction atmosphere at 500 °C on impedance spectra for the CPO_{20} and CeO_2 infiltrated cell, respectively. From Figures 13 and 14, the relaxation at high frequency and the shoulder at medium frequency were not dependent on reaction atmosphere; these peaks could then be associated to oxygen ion transport in the electrolyte and across the electrolyte-electrode interface at TPB. The relaxation at low frequency exhibited an increase in resistance associated to a frequency decrease when propene was introduced into the reactor. This behaviour could be due to oxygen dissociation and transport on the LSM_{15} surface. These suprafacial processes on the electrode were coupled with electrochemical process, as verified by the effect of polarization on resistance in the low frequency arc (Figure 10c and 11c). Propene adsorption on LSM_{15} and CGO_{10} surfaces decreased the

17

rate and interfered with the oxygen exchange reaction on the electrode surface, increasing the resistance of the low frequency peak.

This behaviour was exhibited by the CeO_2 infiltrated cell (Figure 14), as relaxation at high frequency was not affected by the reaction atmosphere. The relaxation at low frequency increased resistance and moved to slightly lower frequencies with the introduction of propene. In the case of CeO_2, this effect was less pronounced than for the CPO_{20} cell (Figure 13). Zheng Y. et al. studied the effect of oxygen vacancies on the oxygen reduction reaction (ORR) on $La_{0.8}Sr_{0.2}MnO_3$ [25]. After a 3 hours cathodic polarization at 800 °C, the size of polarization resistance on impedance spectra reduced significantly because of the *in-situ* generation of oxygen vacancies. The size of low frequency arc increased slightly with the variation of methane partial pressure at constant oxygen partial pressure. These changes were more significant than those before the cathodic polarization but still lower than those generated by oxygen partial pressure change. This experiment demonstrated that oxygen and methane began to have a competitive adsorption on *in-situ* generated oxygen vacancies created by cathodic polarization.

CeO_2 and CPO_{20} are well known oxygen buffers with high oxygen storage/release capacity (OSC) due to the high mobility of lattice defects, like oxygen vacancies. Reddy et al. showed that a ceria-praseodymia system exhibited five times higher OSC than a pure ceria sample [26]. The high OSC of ceria-praseodymia was due to the increased presence of oxygen vacancies respect to CeO_2 and cooperative Ce^{4+}/Ce^{3+} and Pr^{4+}/Pr^{3+} redox couples. For this characteristic the influence of the adsorption of propene on

18

Spectra deconvolution: CPO_{20} infiltrated cell

The spectra were modelled using R(RQ)(RQ)(RQ) and R(RQ)(RQ)G as equivalent circuits at OCV for CeO_2 and CPO_{20} [19]. In this case, the Gerischer element (G) was used to account for the mixed ionic and electronic behaviour of CPO_{20}.

The simulation of the CPO_{20} infiltrated cell was made using two models. The first model with two CPE elements and one Gerischer element was used at temperatures between 500 °C and 400 °C. The second model with three CPE elements was used at temperatures below 400 °C. As reported by Fagg et al. [27], at temperatures close to 350 °C the total conductivity in air for a $Ce_{0.8}Pr_{0.2}O_{2-\delta}$ system showed decreased activation energy as the conductivity became predominantly electronic through the reoxidation of Pr^{3+} to Pr^{4+} with decreasing of oxygen vacancies. The evaluation of the model was based on fitting residuals, accepting the lowest residual as the most reliable fitting. The choice of model was thus based on reaction temperature and was able to take into account the change in ionic conductivity of CPO_{20}. The high frequency process observed in the spectra (ARC1) had activation energy of 0.78 ± 0.06 eV. The arc closed completely at high frequency when the temperature reached 300 °C. The near equivalent capacitance lay between 2.04×10^{-8} F/cm^2 and 2.8×10^{-8} F/cm^2 and was

19

independent of temperature between 500 °C and 350 °C. The independence from temperature and gas phase shift (Figure 13) attributed this arc to the migration of oxygen ions from the electrolyte to the LSM_{15}/CGO_{10} electrode

At 300 °C an increase in the capacitance to 7.5×10^{-8} F/cm^2 was observed. This behaviour could have been due to the overlap of the electrolyte grain boundaries response with the oxygen ion migration. This was not clearly visible in the DRT analysis likely due to the time constants overlap, but it was confirmed by the full closing of the arc at 300 °C. The extraction of the activation energy for this high frequency process was performed using the resistance values obtained at temperatures above 300 °C. The high frequency arc (ARC 1) was slighlty influenced by polarisation at +4 V, an increase in arc resistance for temperatures below 500 °C and a small increase in activation energy (0.86 ± 0.1 eV) were observed. At the same time the near equivalent capacitance increased to 3.2-4.1×10^{-8} F/cm^2.

The process belonging to the medium frequency region (ARC 2) had an activation energy of 0.58 ± 0.1 eV and a near equivalent capacitance that increased with temperature from 2.2×10^{-4} F/cm^2 at 300 °C to 5×10^{-4} F/cm^2 at 500 °C. This arc showed a slight dependence on reaction atmosphere and due to the increase of capacitance with the temperature, this arc could be correlated to the adsorption, diffusion or charge transfer at or near the three-phase boundary (i.e., increasing temperature will increase the TPB zone and thereby increase the associated capacitance). This part of the spectrum was fitted with a CPE element having n-values between 0.45 and 0.53 depending on the temperature. The slope of this arc, the ratio of $-Z^{''}$ and $Z^{'}$, calculated from the Nyquist plot increased with increasing temperature from

20

0.25 to 0.5. The distorted shape of the medium frequency arc was explained by the porous structure of the electrode. For an electrode-process described by an R-CPE parallel circuit, the impedance response in a porous electrode will be approximated by the square root of the impedance of the R-CPE element [28]:

$$Z_{\mathrm{R-CPE,porous}} = \sqrt{Z_{\mathrm{R-CPE}}}$$

In Figure 10b, the application of +4 V was able to strongly affect ARC 2 and ARC 3, reducing them to a single process/arc. In this case it was possible to observe from the Nyquist plot in Figure 10b two well separated arcs over the entire spectra. The low frequency arc was associated to a two orders of magnitude increase in peak characteristic frequency and to a near equivalent capacitance of 4.9-9.4 10^{-5} F/cm^2, but the dependence on temperature was not clear. The capacitance increased with decreasing temperature until 400 °C, and then decreased again at 350 °C and 300 °C. The polarisation decreased capacitance by one order of magnitude with respect to OCV. The second arc clearly lost its characteristic slope during polarisation. In this case, the n-value of the CPE used was between 0.59 and 0.64. The new arc formed under polarization had an activation energy of 0.59 ± 0.07 eV, similar to the value obtained at OCV. We could therefore argue that the polarisation only affected the third arc. ARC 3 was modelled using two different elements. At temperatures of 350 °C and 300 °C, an RQ element was used to simulate this arc. The spectra for both temperatures did not close at lower frequencies, complicating the fitting. This arc was strongly influenced by reaction atmosphere, had an activation energy of 0.79 ± 0.06 eV and a near equivalent capacitance of 2.6-2.8 × 10^{-3} F/cm$^{2.}$ At temperatures between 400 °C and 500 °C, an RG element was used to simulate the spectra. Such an impedance

response has been argued to arise in both mixed electronic and ionic conductors, such as LaSrCoO$_3$, and in LSM/YSZ when cathodically polarised. This characteristic was not visible on CeO$_2$ infiltrated cell spectra, so it was possible that this behaviour was a result of CPO$_{20}$ infiltration where oxygen ion diffusion through CPO$_{20}$ was coupled with oxygen ion discharge at the extended TPB.

In mixed ionic electronic conductor cathodes, oxygen ion diffusion is argued to occur primarily along bulk paths, giving high capacitance values near 1 F/cm^2 [29]. In this study, the capacitance was found to be 1.1×10^{-3} F/cm^2 at 500 °C and increased to 3.5×10^{-3} F/cm^2 at 400 °C. These values were far from values found by Adler [29] (1 F/cm^2). A value of 100 μF was also found by Hjalmarsson et al. using LaCoNiO$_3$-CeGdO and attributed to oxygen transport confined to the electrode surface rather than the bulk [30]. Oxygen ion diffusion could follow two different paths: along the electrode surface (LSM$_{15}$) or along bulk paths (CPO$_{20}$). The activation of the resistance, R_G, associated to a Gerischer element was found to be 0.44 ± 0.05 eV.

Spectra deconvolution: CeO$_2$ infiltrated cell

The spectra of the CeO$_2$ infiltrated cell were modelled using 3 CPE elements in series with a resistance R(RQ)(RQ)(RQ) for all temperatures. The spectra at 350 °C and 300 °C recorded at OCV also did not close at low frequencies. The first process at high frequencies visible in DRT analysis of Figure 12 was associated to the first arc (ARC 1). The activation energy of this arc was 1.14 ± 0.15 eV at OCV and was surprisingly higher than the value obtained for the CPO$_{20}$ cell. The difference in ARC 1 resistance between

22

CeO$_2$ and CPO$_{20}$ cells is mainly visible for temperatures between 400 °C and 300 °C and not for higher temperatures. This behaviour is confirmed by DRT analysis of Figure 12, Figure 13 and 14 where the two cells show a similar resistance for the relaxation contribution at high frequency.

The application of +4 V polarisation had no effect on the resistance of this arc with an observed activation energy of 1.13 ± 0.08 eV. It was thus possible to infer that also this part of the spectra could be influenced by the infiltration material especially at medium-low temperature and could contain overlapping processes. This overlap would complicate separation of two close relaxation times belonging to the infiltrated material and the backbone.

As verified for CPO$_{20}$, the near equivalent capacitance of this arc was almost unaffected by temperature both at OCV and at +4 V (values between 4.5 and 4.7 × 10^{-8} F/cm^2). At 300 °C, where the first arc was fully closed on the high frequency side, the capacitance dropped to 2.9 × 10^{-8} F/cm^2. At this temperature it was possible to measure the electrolyte grain boundaries contribution to conductivity. Additionally, this arc was not affected by reaction atmosphere. Analysing its characteristics, this arc was attributed to the migration of oxygen ions from the electrolyte to the LSM$_{15}$/CGO$_{10}$ electrode.

As observed for CPO$_{20}$, the polarization effect for the CeO$_2$ infiltrated cell was also visible on the second/third arc (ARC 2-ARC 3) and associated to a strong decrease in resistance and increased peak frequency (Figure 11c and 11b). This part of the spectrum was modelled with two RQ at OCV. For ARC 2 (Figure 11a), n-values used for the fitting ranged from 0.49 to 0.68 and the activation energy was 0.79 ± 0.03 eV.

23

The near equivalent capacitance increased from 1.3 to 2.1 $\times$ 10^{-4} F/cm^2 with increasing temperature. In addition, this arc was also affected by the infiltration material. The two modelled arcs visible at OCV merged into one when the cell was polarized at +4 V (Figure 11b). The activation energy measured at +4 V was 1.11 ± 0.06 eV with only one arc observable at this voltage, and contrary to CPO$_{20}$, this activation energy likely belonged to a different process. The near equivalent capacitance increased from 5.2 $\times$ 10^{-5} F/cm^2 at 300 °C to 8 $\times$ 10^{-5} F/cm^2 at 500 °C. The polarization, as observed for CPO$_{20}$, was able to decrease the capacitance by one order of magnitude. The temperature dependence, the polarisation effect and the insensitivity to atmosphere (Figure 14) assigned this arc to the charge transfer near or at the TPB.

The third arc (ARC 3) was only modelled and visible at OCV. This arc was affected by reaction atmosphere, as shown in the DRT analysis of Figure 14, and by temperature with an activation energy of 0.98 ± 0.04 eV. The near equivalent capacitance strongly increased with temperature from 8.6 $\times$ 10^{-5} F/cm^2 at 300 °C to 5.7 $\times$ 10^{-4} F/cm^2 at 500 °C. This process was thus related to the adsorption and dissociation of oxygen, as well as electrode reaction, on the catalyst/electrode surface.

For both infiltrated material, ARC 1 was attributed to oxygen ion transport between the electrolyte and LSM and to grain boundary conductivity; these processes were not faradaic. The strong resistance decrease upon polarization of ARC 2 and ARC 3 indicated that medium and high frequency part of the spectra contained a charge transfer contribution following the Butler-Volmer equation. This behaviour did not exclude the possibility that chemical/physical processes could contribute to the total resistance; these processes, if associated to an electrochemical process, can exhibit

the general Butler-Volmer behaviour [31]. According to C.J. Borja, [32] ARC 2 could be tentatively attributed to the charge transfer reaction taking place at the three phase boundaries:

$$O^{2-} \rightarrow O_{(TPB)} + 2e^-$$
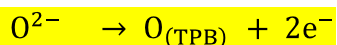
The oxygen formed at TPB could undergo different reactions: it could recombine to form molecular oxygen, react with adsorbed propene giving rise to an increase of reaction rate or migrate over the entire gas-exposed catalyst electrode surface establishing an effective double layer able to increase the reaction rate above the faradaic limit (EPOC).

The ARC 3 was the most affected by introduction of propene in the gas mixture as also reported by Butlel with Pt/YSZ system [33]. Propene was strongly adsorbed on electrode surface; it is possible to argue that the introduction of propene could interfere with a process involving biatomic oxygen or dissociated oxygen on the surface. Kaloyannis et al. [34] reported a competitive adsorption mechanism of dissociative chemisorbed oxygen and propylene during electrochemical promotion studies with stronger binding of propylene than oxygen on the Pt catalyst surface. As illustrated before, the sensitivity to propene introduction was dependent on infiltrated material and especially on its oxygen vacancies mobility.

Upon applying positive potential the increase in catalyst work function is obtained primarily by the increase in the coverage of the backspillover oxide ions $O^{\square-}$; the effects should be to enhance the reactivity of surface oxygen species coming from the gas phase and changing the adsorption strength of the adsorbates like oxygen and propene. The effect of polarization on impedance spectra in this work was visible at medium and

low frequency associated to one order of magnitude decrease of both resistance and capacitance; the impedance spectra recorded under polarization did not show any new semicircle with high capacitance (> 200 µF/cm^2) as reported by Vayenas et al. [35] and attributed to backspillover oxygen semicircle. In this work EPOC behavior was not visible, probably due to the fast reaction of oxygen ions with another oxygen or with propene; the short lifetime of the oxygen ions hindered the possibility to the effective double layer formation between the catalyst and the gas phase. Kambolis et al. [36] did not observe EPOC in propane oxidation on LSCF/GDC electrode but it was observed on Pt infiltrated LSCF/GDC electrode, especially at low temperature (267 °C). The impregnation of Pt had two effects: increase the reaction rate towards propane oxidation at OCV and also the electrode polarization resistance (R_p) measured at OCV. These two combined effects gave rise to EPOC behavior.

Conclusions

The catalytic activity of a CeO_2 infiltrated cell in propene oxidation was shown to be superior to a CPO_{20} system. The performance in terms of polarization effect on propene oxidation was strongly influenced by electrochemical and electrical properties of the infiltrated material. CeO_2 infiltrated cell exhibited high electrode resistance if compared to CPO_{20}. The activity of CeO_2 in propene oxidation was highly influenced by polarization, especially at low temperatures, and displayed good faradaic efficiency. The low electrode resistance of $CPO_{20,}$ instead, was detrimental to obtain good faradaic

26

efficiency at low temperature, likely due to the short lifetime of oxygen ion promoters given by mixed conductivity of CPO_{20}.

Impedance spectra exhibited three main features belonging to oxygen ion migration/grain boundary conductivity, charge transfer reaction of oxygen ion and O_2 adsorption/dissociation on the electrode surface. The spectra recorded under anodic polarization showed a strong decrease of resistance and capacitance at medium-low frequency range while the contribution at high frequency was unaffected.

The introduction of propene in the reaction atmosphere affected the low frequency contribution on impedance spectra; CPO_{20} was affected on a major extent, probably due to the higher oxygen vacancies mobility compared to CeO_2. EPOC behaviour was not visible for both the infiltrated cells; the backspillover of oxygen ions was hindered by the high reactivity of the oxygen promoter at the TPB.

Acknowledgements

Captions

Fig. 1: Scheme of the reactor configuration.

Fig. 2: SEM micrograph of a CeO_2 infiltrated cell.

Fig. 3: SEM micrograph of a CPO_{20} infiltrated cell.

Fig. 4 : XRD powder pattern of CPO_{20} powder.

Fig. 5: Reaction rate for propene oxidation as a function of temperature in 1000 ppm C_3H_6 and 10% O_2 at 2 L/h.

Fig. 6: Rate enhancement ratios of CeO_2 and CPO_{20} infiltrated cells as a function of temperature.

Fig. 7 : Faradaic efficiency of CeO_2 and CPO_{20} infiltrated cells versus temperature.

Fig. 8: Arrhenius plots of polarisation resistance (R_p) at OCV for CeO_2 and CPO_{20} infiltrated cells.

Fig. 9: Arrhenius plots of polarization resistance (R_p) at +4 V for CeO_2 and CPO_{20} infiltrated cells.

Fig. 10: Nyquist plots of impedance spectra of a CPO_{20} infiltrated cell recorded at a) OCV, b) +4 V and c) Bode plot of impedance spectra at 450 °C and OCV with 10% O_2 and 1000 ppm C_3H_6 at 2 L/h.

29

Fig. 11: Nyquist plots of impedance spectra of a CeO_2 infiltrated cell recorded at a) OCV, b) +4 V and c) Bode plot of the impedance spectra as a function of frequency at 450 °C and OCV with 10% O_2 and 1000 ppm C_3H_6 at 2 L/h.

Fig. 12: Distribution of relaxation times (DRT) for CeO_2 and CPO_{20} spectra recorded at 450 °C and OCV with 10% O_2 and 1000 ppm C_3H_6 at 2 L/h.

Fig. 13: Distribution of relaxation times (DRT) in the CPO_{20} spectra recorded at 500 °C and OCV with 10% O_2 and 10% O_2 + 1000 ppm C_3H_6 at 2 L/h.

Fig. 14 : Distribution of relaxation times (DRT) in the CeO_2 spectra recorded at 500 °C and OCV with 10% O_2 and 10% O_2 + 1000 ppm C_3H_6 at 2 L/h.

References

1. Wiartalla A, Ruhkamp L, Rosefort Y, Maassen B, Sliwinsky B, Schornbus T, Laible T (2011) SAE International 2011-01-2097
2. Miller Kristin A (2007) N Engl Med 356:447-458
3. Oberdoster G (2004) Inhalation Toxicol 16:437–445
4. Jonhson TV (2011) SAE International 2011-01-0304
5. Choudhary TV, Banerjee S, Choudhary V R (2002) Appl Catal A 234:1-23.
6. Yamazoe N, Teraoka Y (1990) Catal Today 8:175-199
7. Seyama T (1992) Catal Rev-Sci Eng 34:281-300
8. Spinicci R, Faticanti M, Marini P, De Rossi S, Porta P (2003) J Mol Catal 197:147-155
9. Stoukides M, Vayenas C G (1981) J Catal 70:137-146
10. Gaillard F, Li X, Uray M, Vernoux P (2004) Catal Lett 96:177-183

11. Roche V, Siebert E, Steil MC, Deloume JP, Roux C, Pagnier T, Revel R, Vernoux P (2008) Ionics 14:235-241

12. Tsiakaras P, Athanasiu C, Marnellos G, Stoukides M, ten Elshof JE, Bouwmeester HJM (1998) Appl Catal A 169:249-261

13. Balomenou SP, Tsiplakides D, Vayenas CG, Poulston S, Houel V, Collier P, Konstandopoulos AG, Agrafiotis C (2007) Top in Catal 44:481-486.

14. Twigg MV (2007) Appl Catal B 70:2-15

15. Zhao S, Gorte RJ (2003) Appl Catal A 248:9-18

16. Werchmeister RML, Hansen KK, Mogensen M (2010) Mat Res Bull 45:1554-1561

17. Schichlein H, Muller AC, Voigts M, Krugel A, Ivers-Tiffée E (2002) J Appl Electrochem 32:875-882

18. Kharton VV, Viskup AP , Figueiredo FM, Naumovich EN, Shaulo AL, Marques FMB (2002) Mater Lett 53:160-164

19. Ippolito D, Andersen KB, Hansen KK (2012) J Electrochem Soc 159:P1-P8

20. Putna ES, Vohs JM, Gorte RJ, Graham GW (1998) Catal Lett 54:17-21

21. Zhao S, Gorte J (2004) Appl Catal A 277:129-136

22. Mogensen M, Sammes NM, Tompsett GA (2000) Solid State Ionics 129:63-94

23. Endler C, Leonide A, Weber A, Tietz F, Ivers-Tiffée E (2010) J Electrochem Soc 157:B292-B298

24. Boukamp BA, Verbraeken M, Blank DHA, Holtappels P (2003) Solid State Ionics 157:29-33

25. Zheng Y, Ran R, Qiao SZ, Shao Z (2012) Int J Hydrogen Energy 37:4328:4338

26. Reddy BM, Thrimurthulu G, Katta L, Yamada Y, Park SE (2009) J Phys Chem C 113:15882-15890

27. Fagg DP, Perez-Coll D, Nunez P, Frade JR, Shaula AL, Yaremchenko AA, Kharton VV (2009) Solid State Ionics 180:896-899

28. Barsoukov E, Macdonald JR (2005) Impedance Spectroscopy. 1st edn. Wiley

29. Adler SB (1998) Solid State Ionics 111:125-134

30. Hjalmarsson P Mogensen M (2011) J Power Sources 196:7237-7244

31. Kim Jd, Kim GD, Moon JW, Park Yi (2001) Solid State Ionics 143:379-389

32. Borja CJ, Dorado F, de L.Consuegra A, Vargas JMG, Valverde JL 2011 Fuel Cell 1:131:139

33. Bultel L, Henault M, Roux C, Siebert C, Beguin B, Gaillard F, Primet M, Vernoux P (2002) Ionics 8:136:141

34. Kaloyannis A, Vayeans CG (1999) Journal of Catalysis 182:37-47

35. Frantzis AD, Bebelis S, Vayenas CG (2000) 136-137:863-872

36. Kambolis A, Lizzaraga L, Tsampas MN, Burel L, Rieu M, Viricelle JP, Vernoux P (2012) Electrochem Commun 19:5-8

Figure 1
Click here to download high resolution image
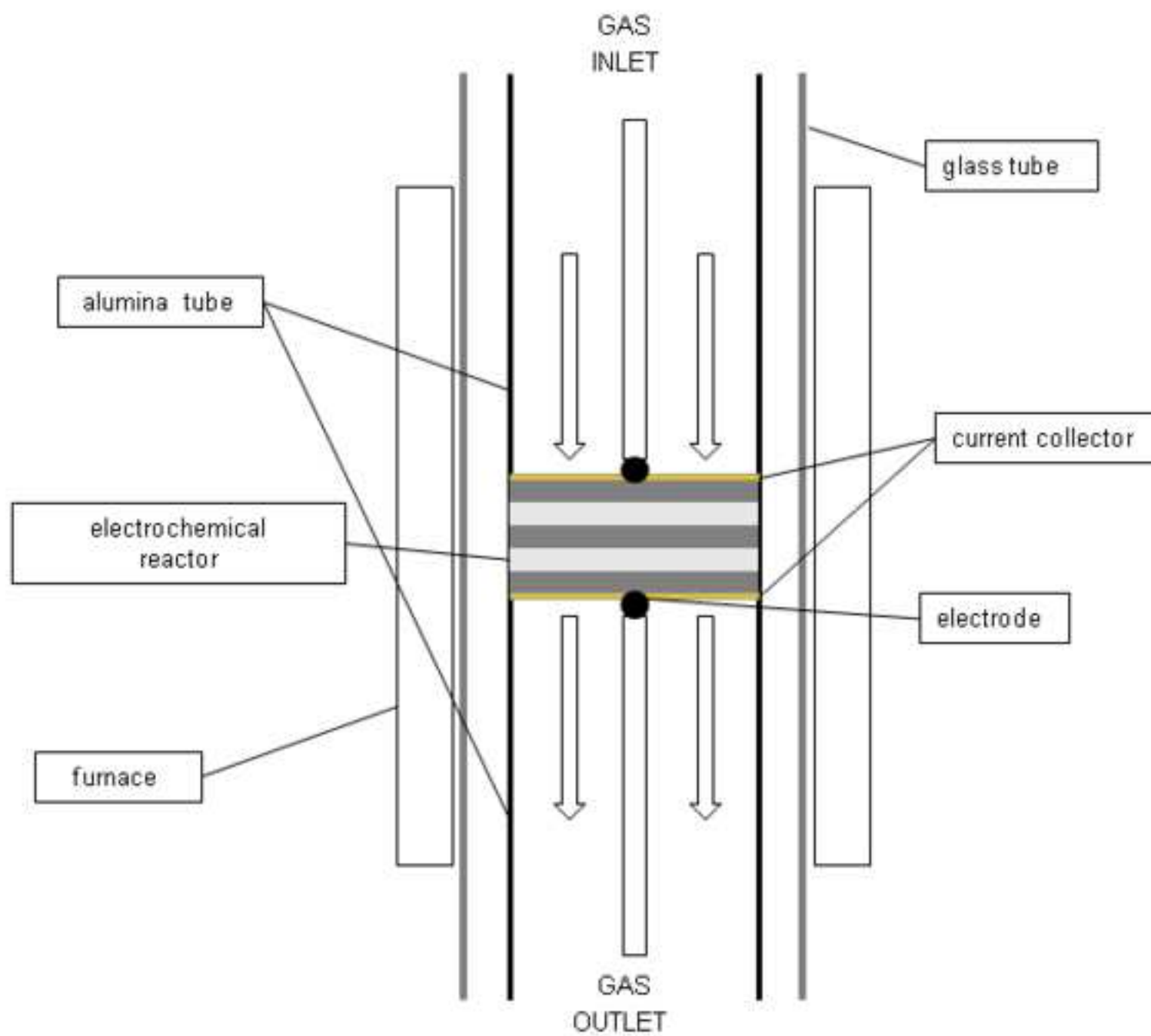
GAS
INLET

glass tube

alumina tube

current collector

electrochemical
reactor

electrode

furnace

GAS
OUTLET
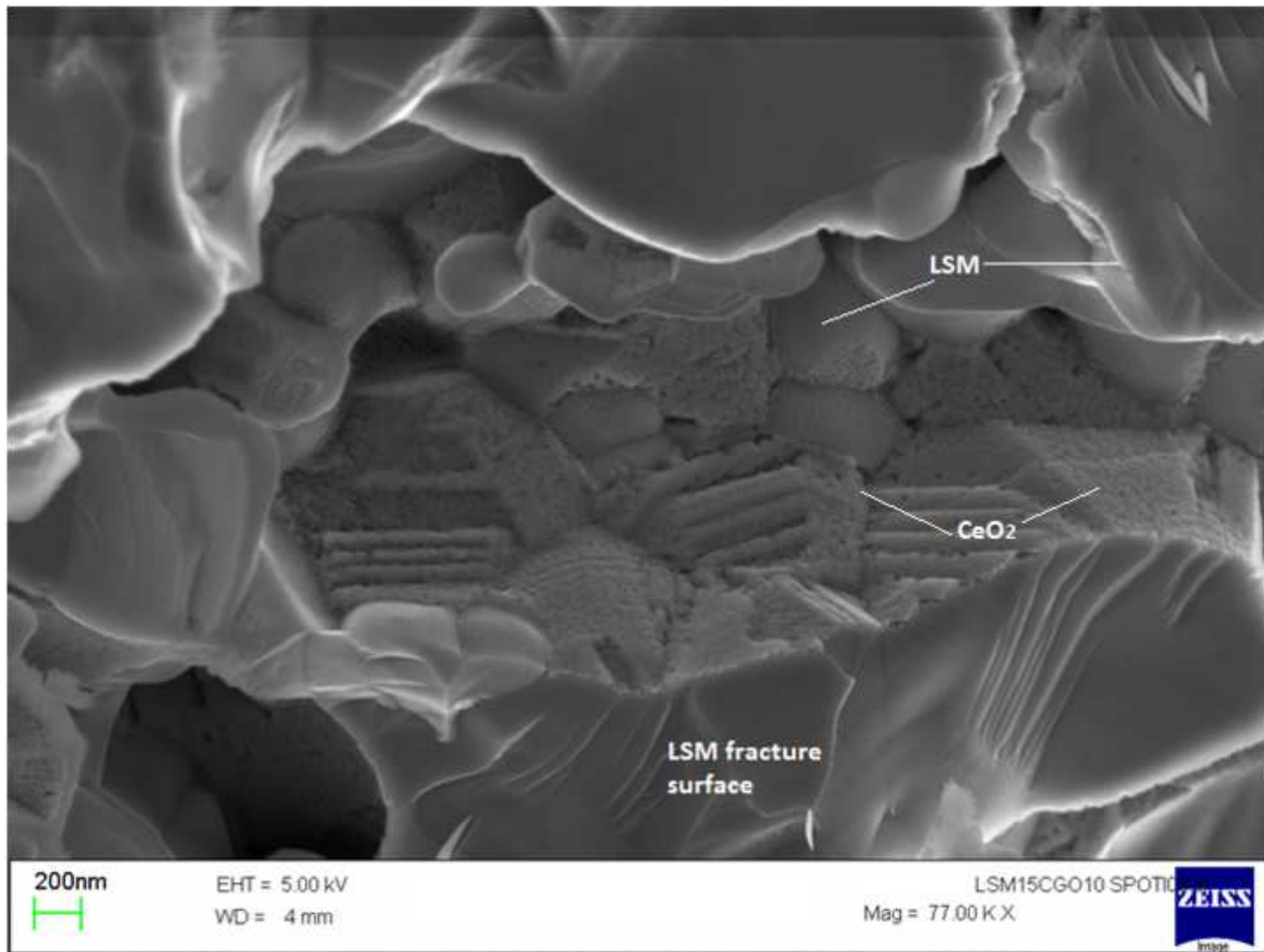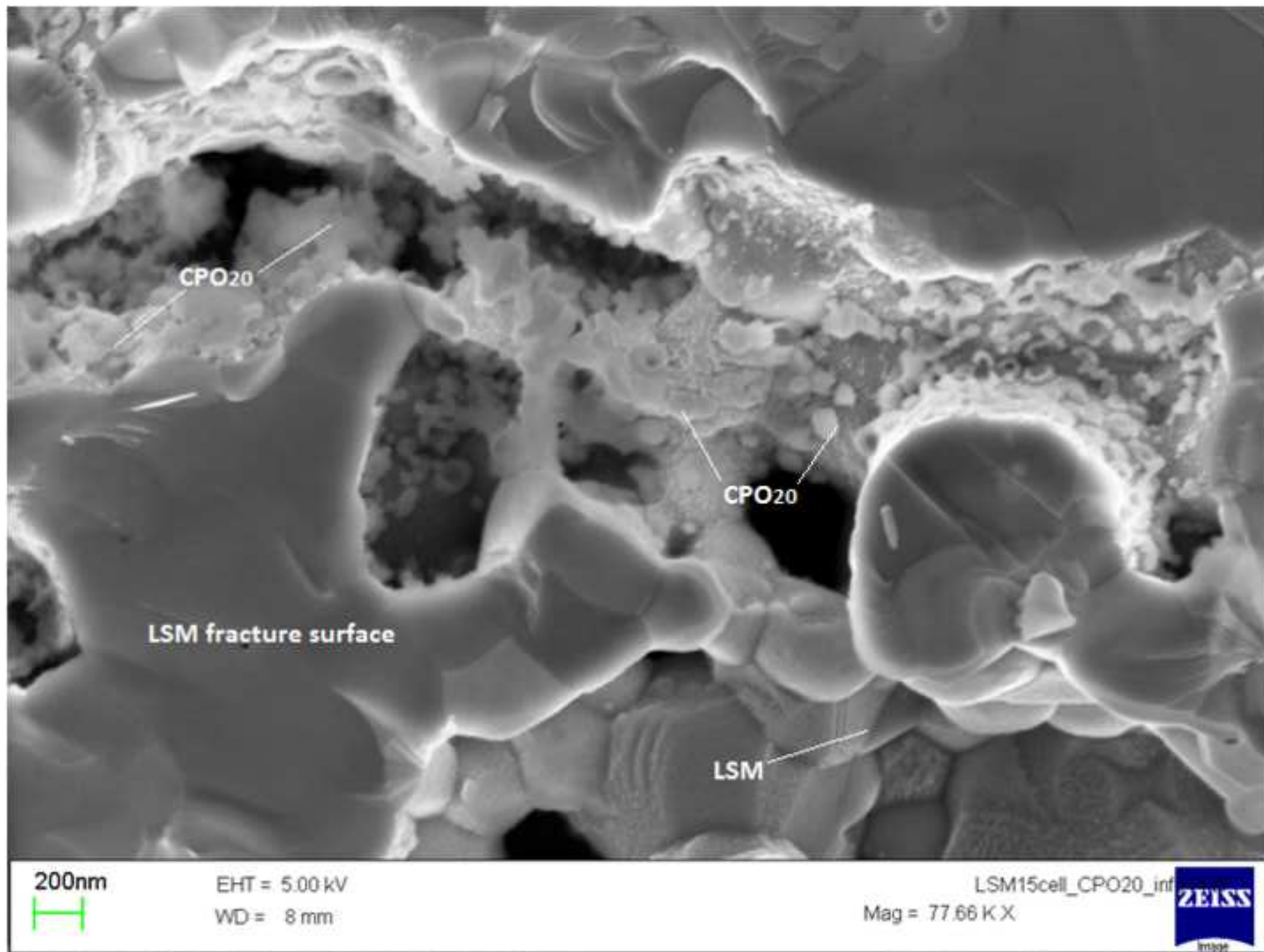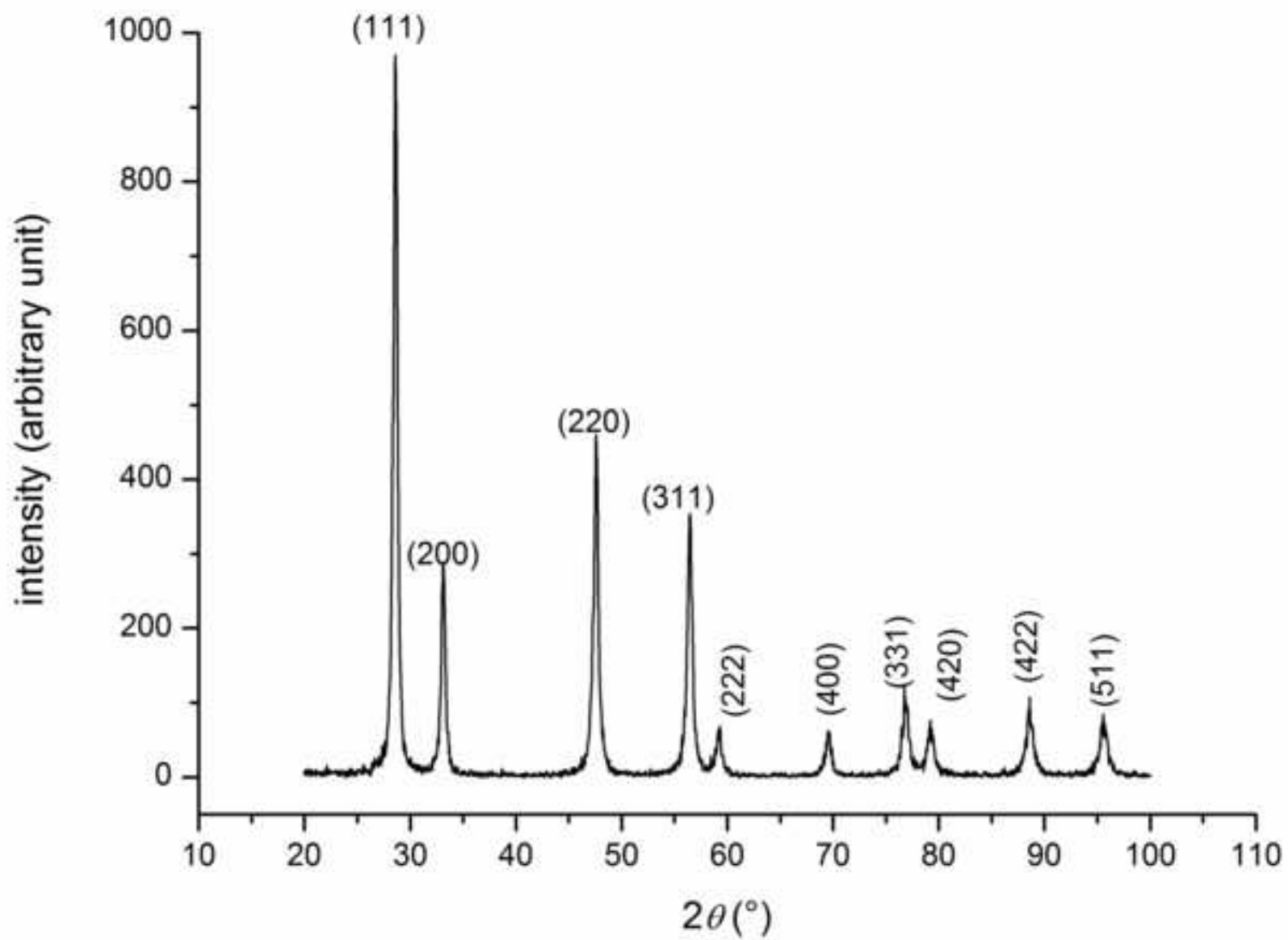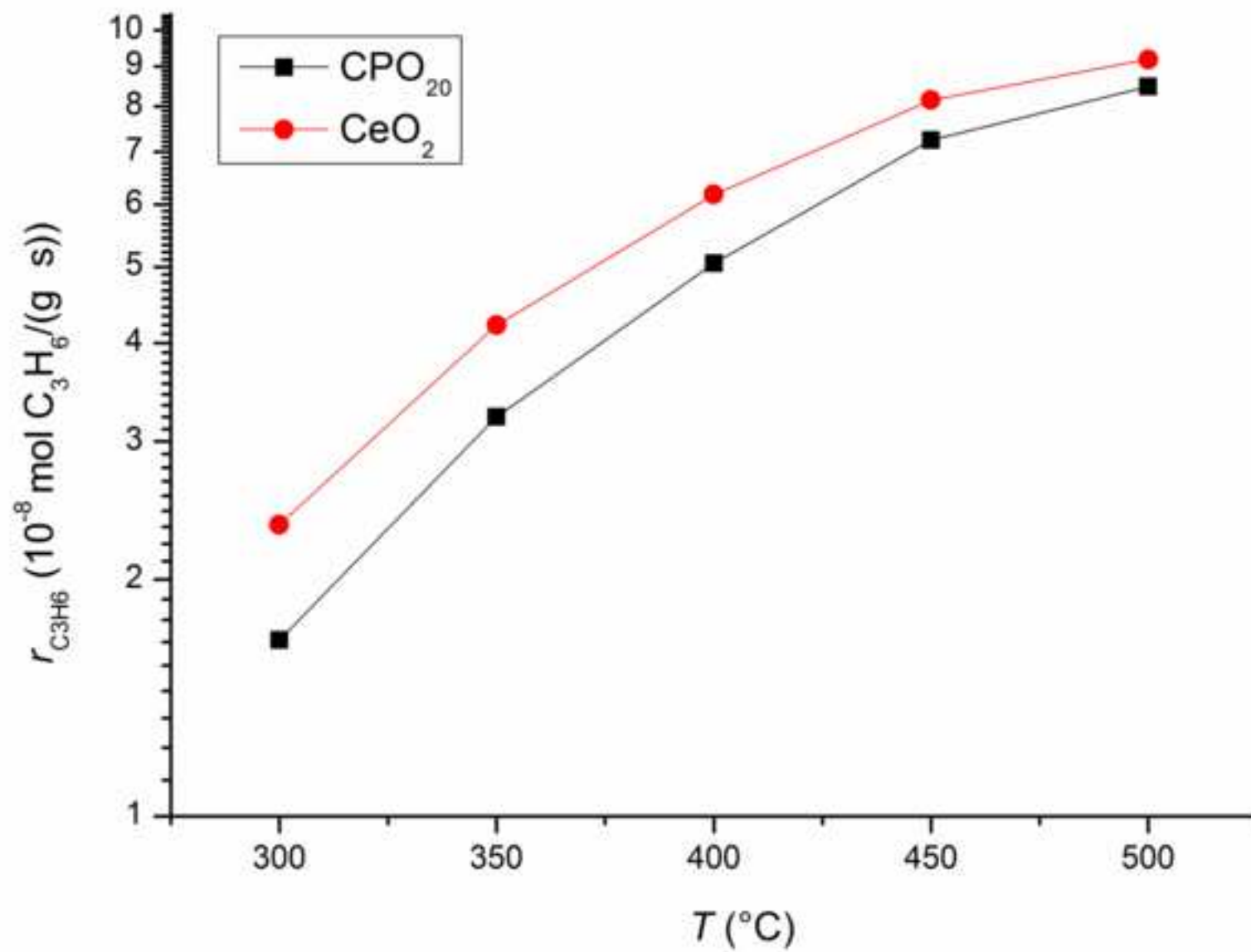
Figure 2

Figure 3
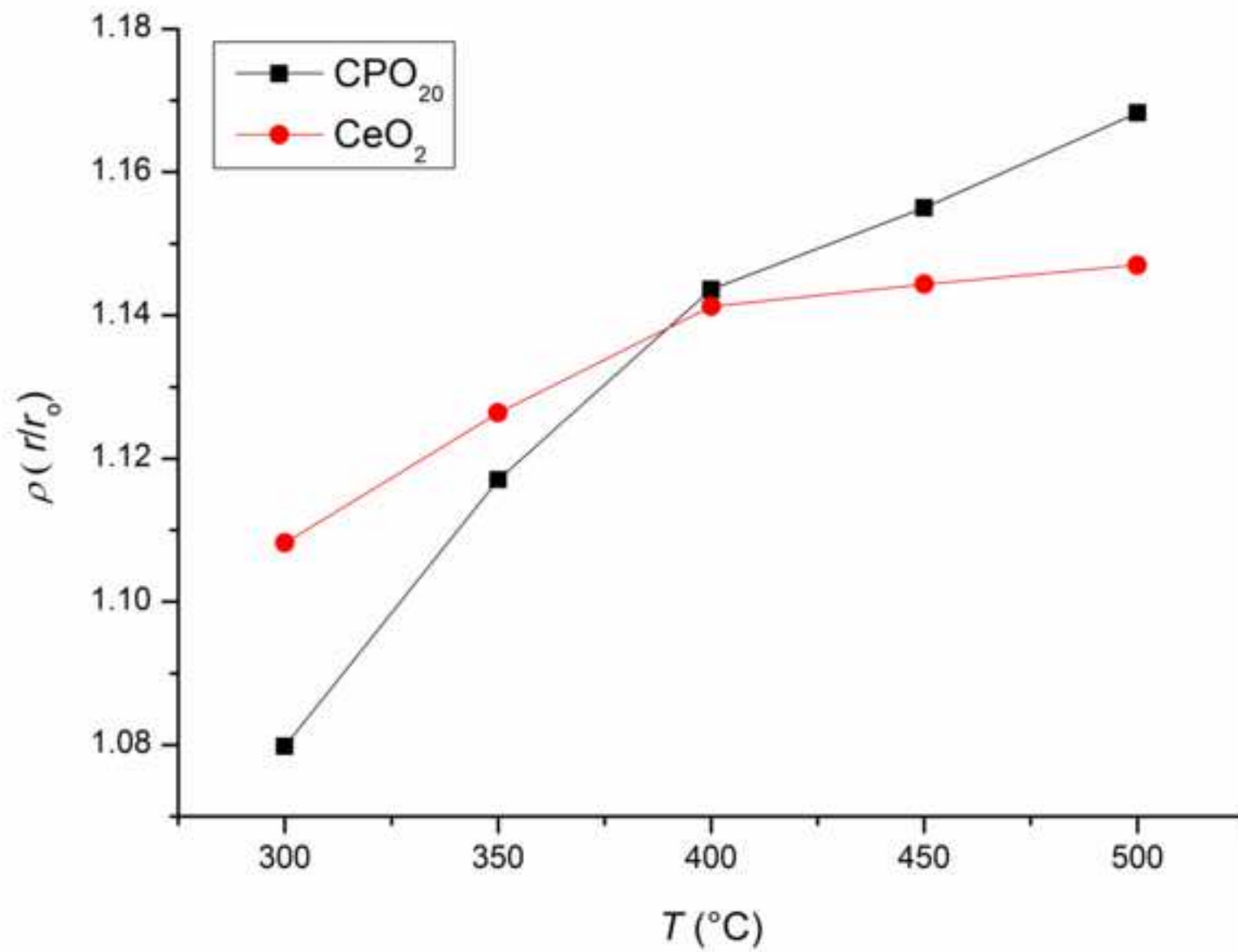
Figure 5

Figure 6
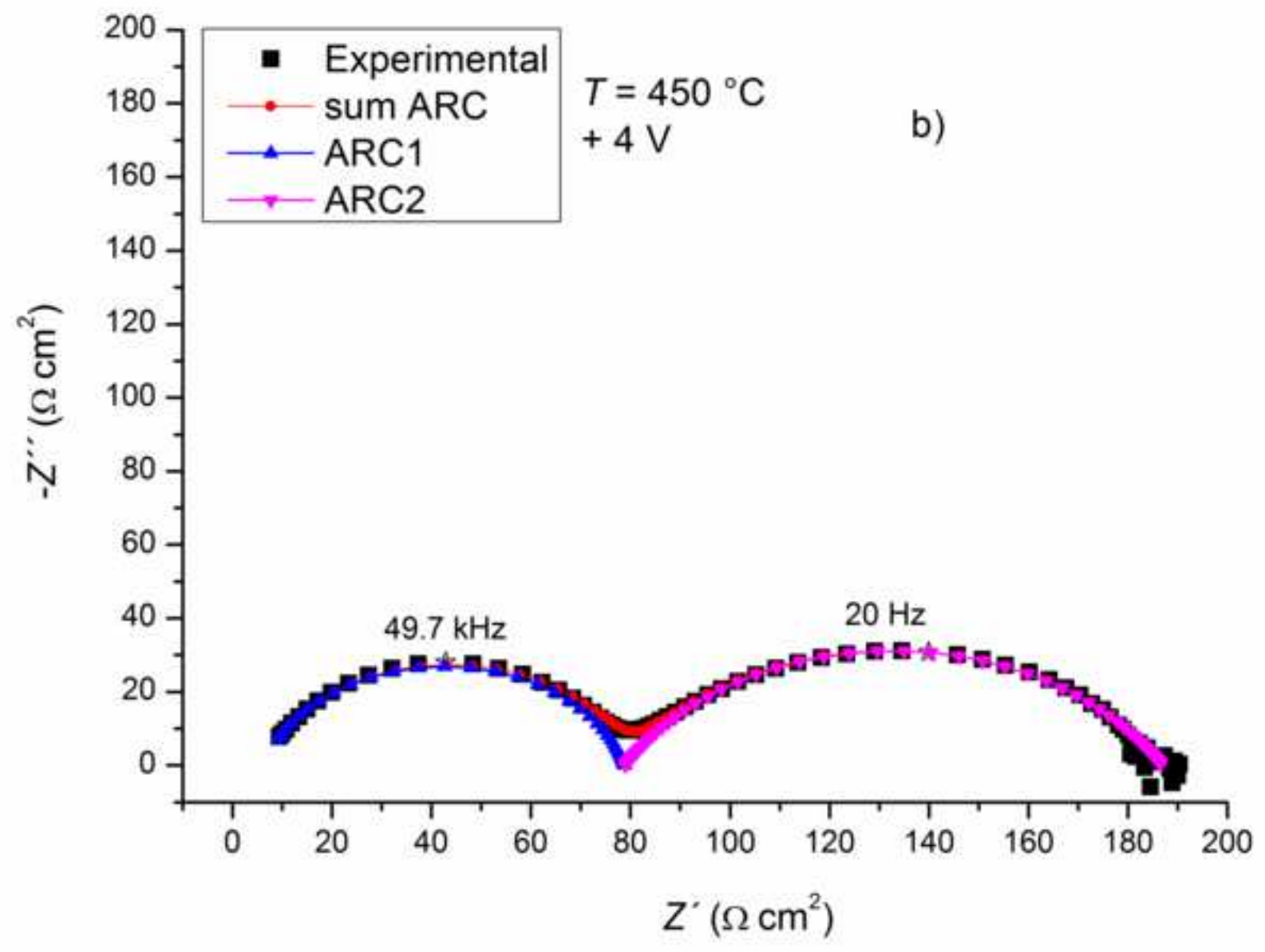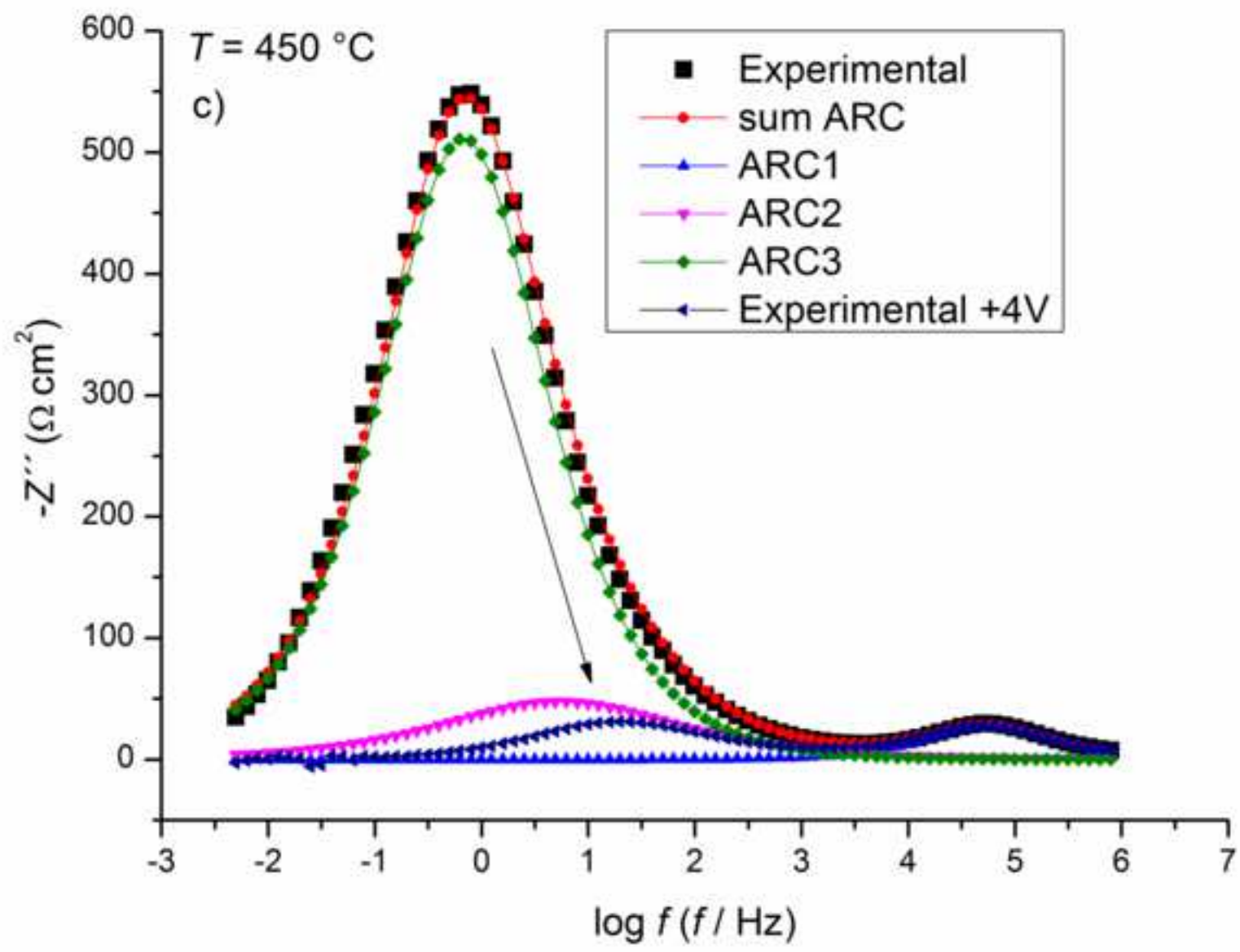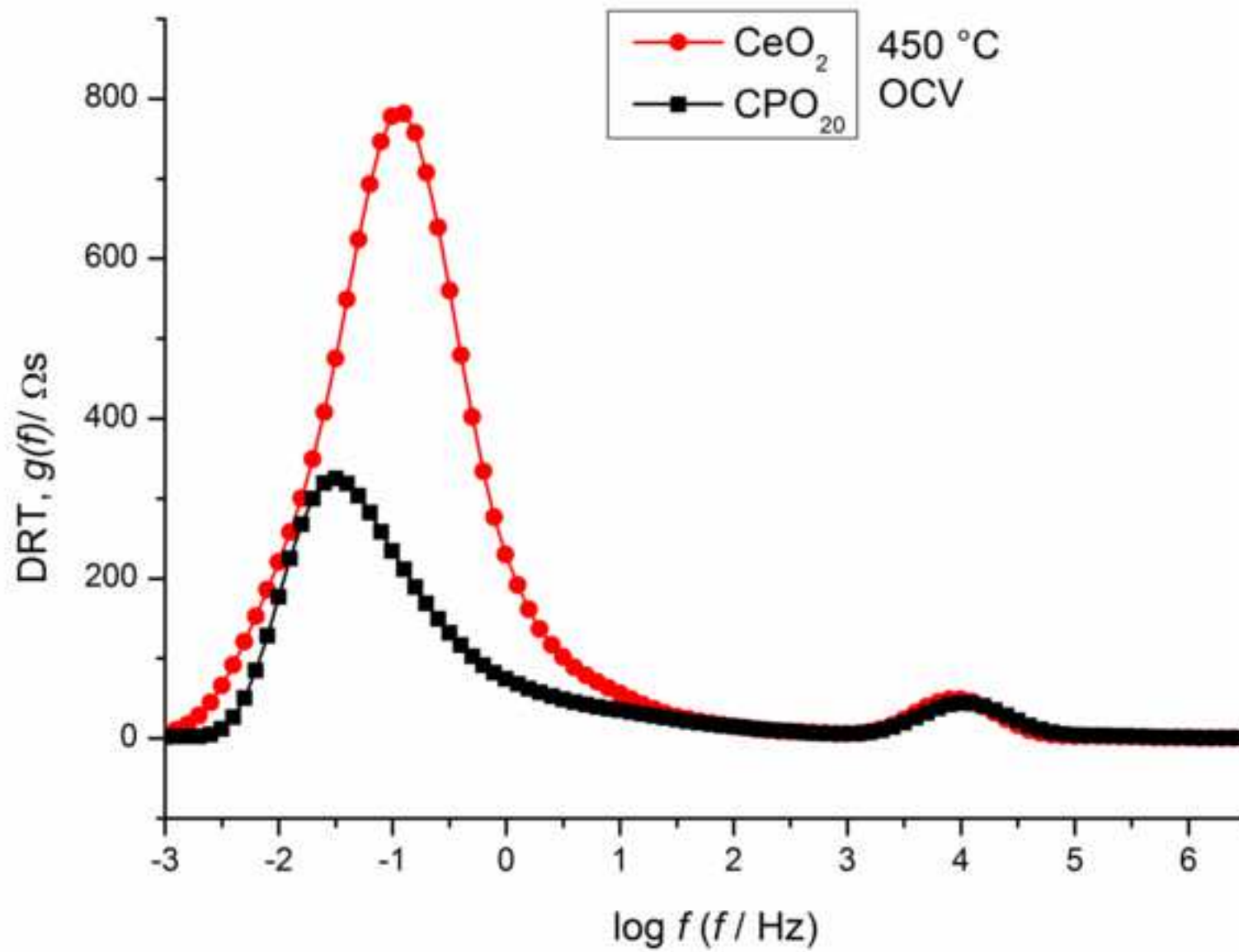
Figure 7
Click here to download high resolution image
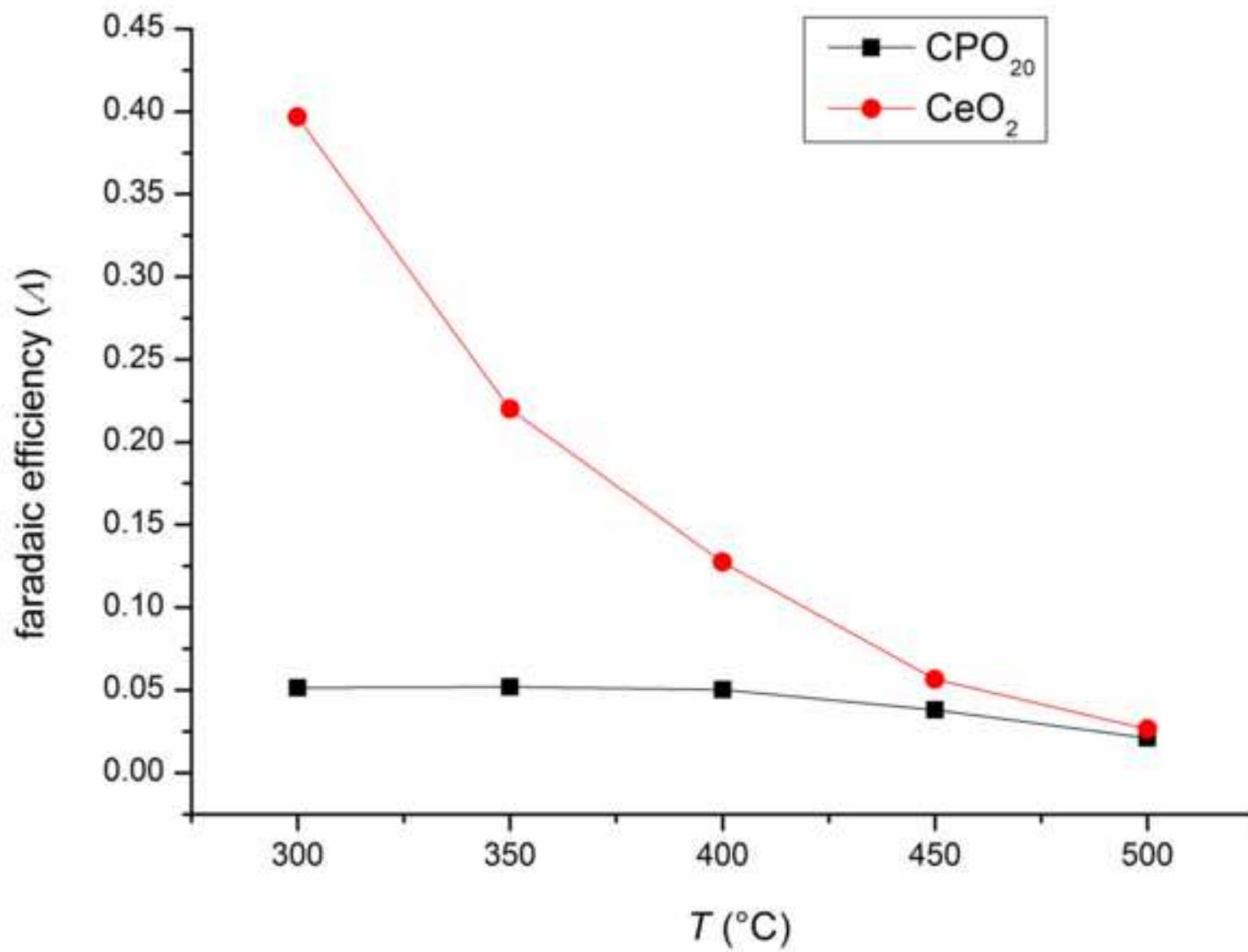
Figure 8
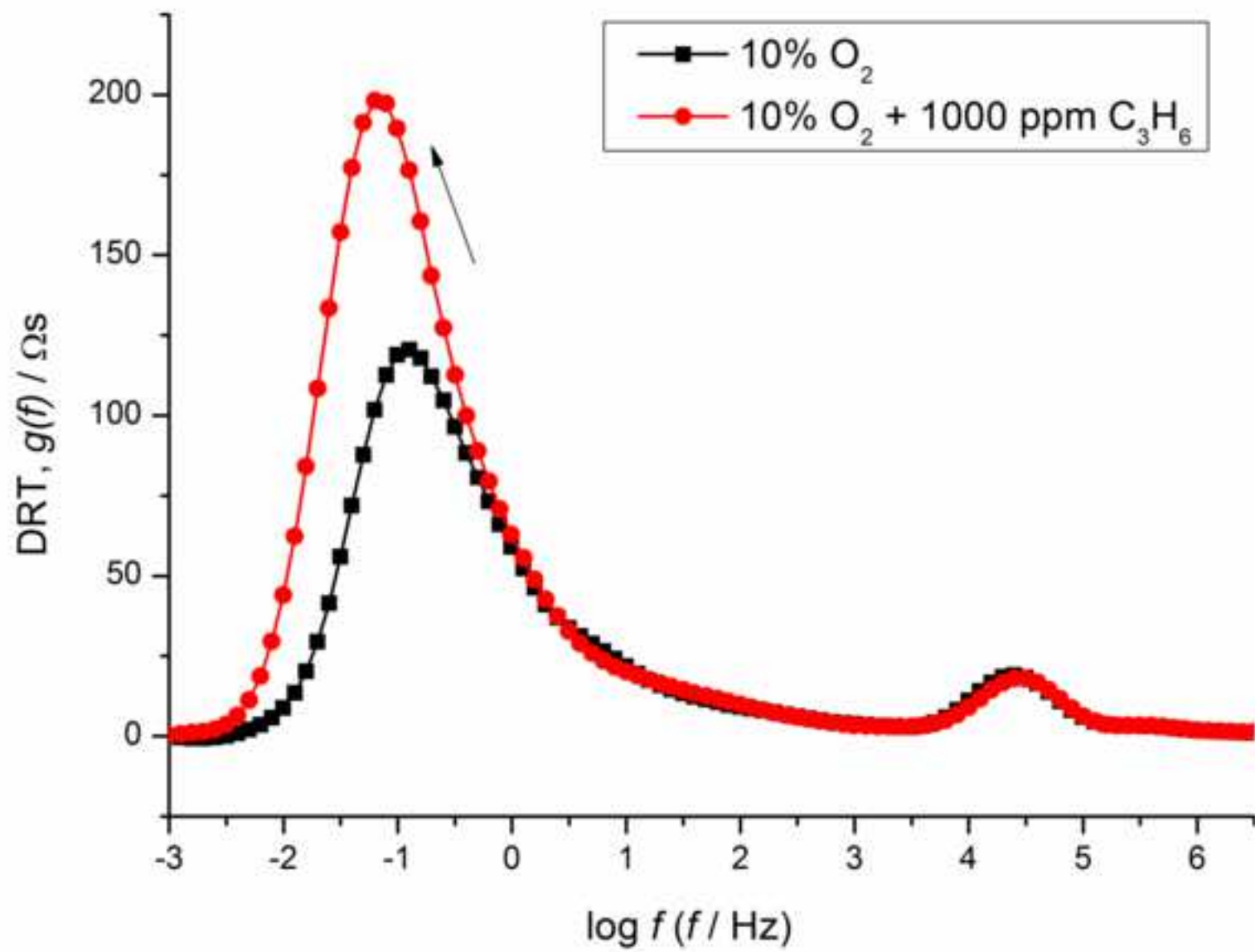Click here to download high resolution image
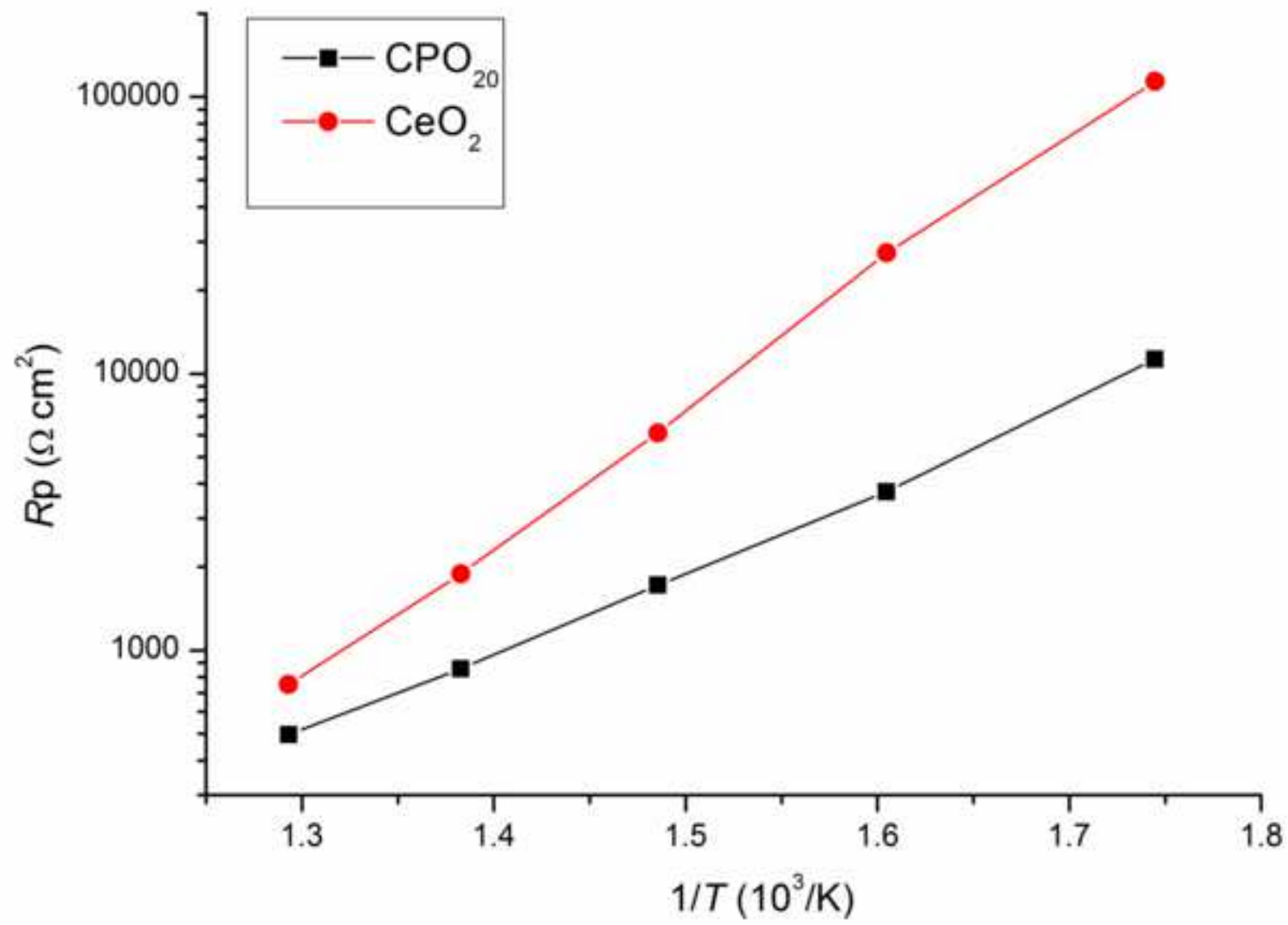
Figure 9
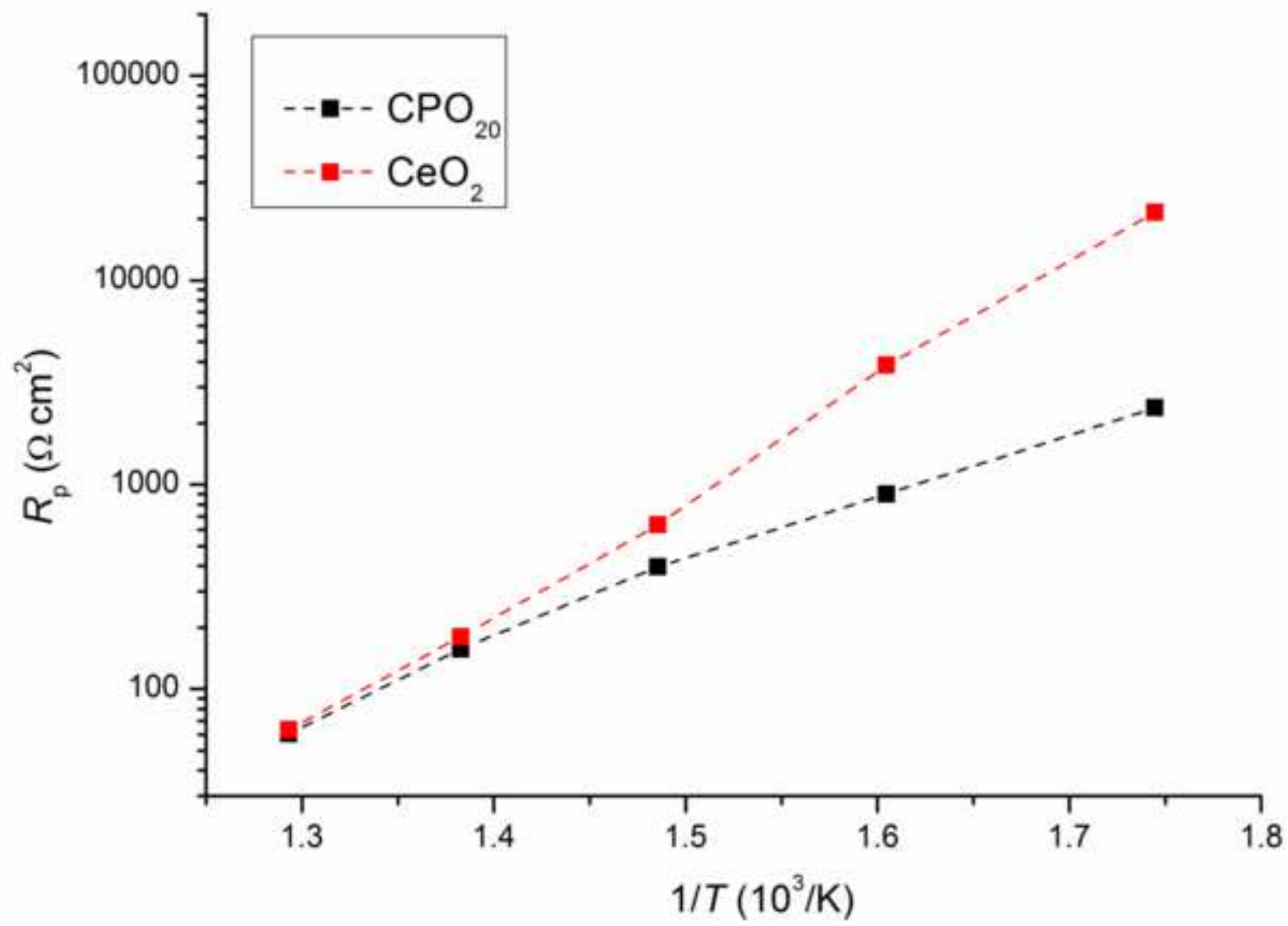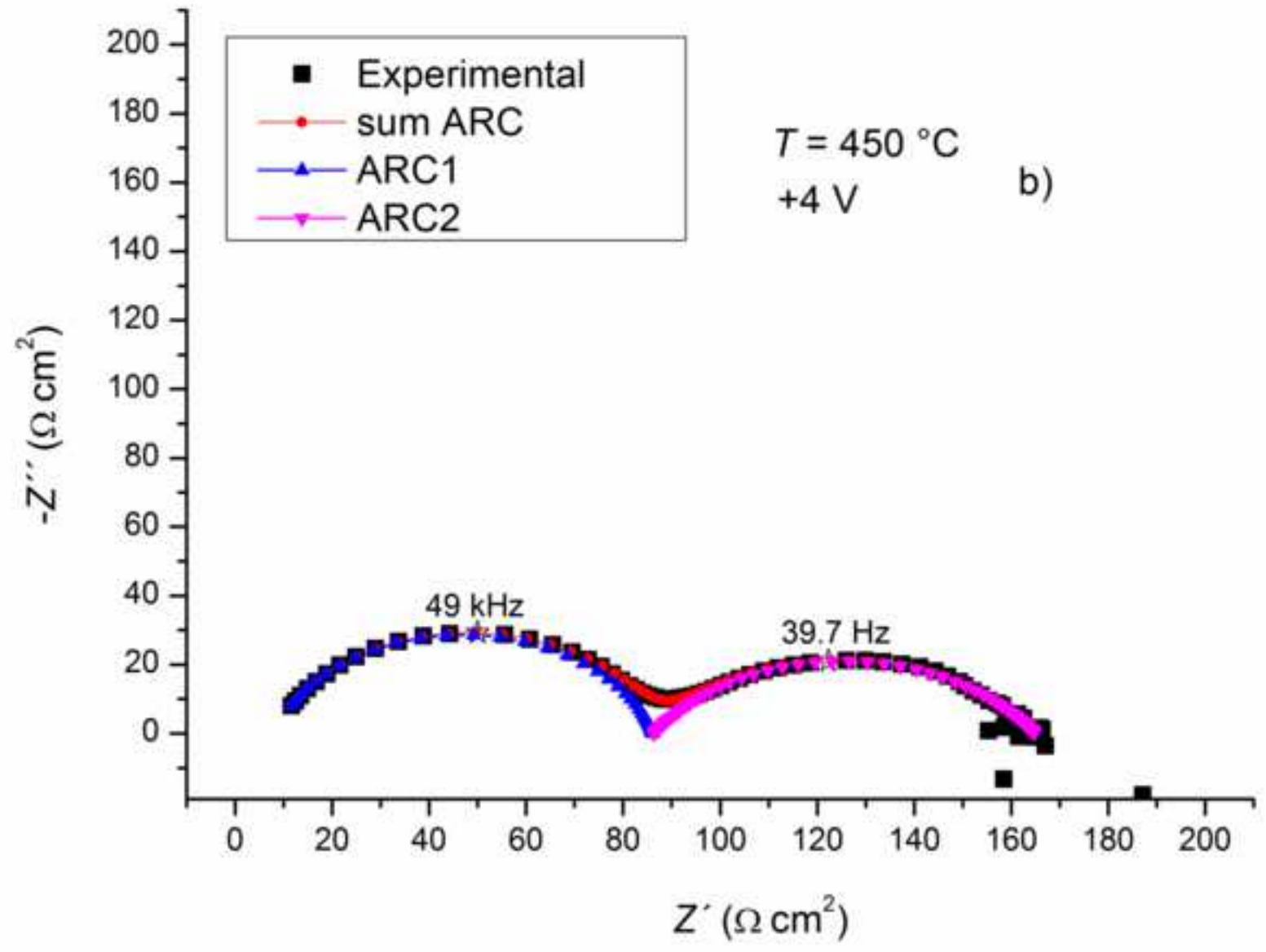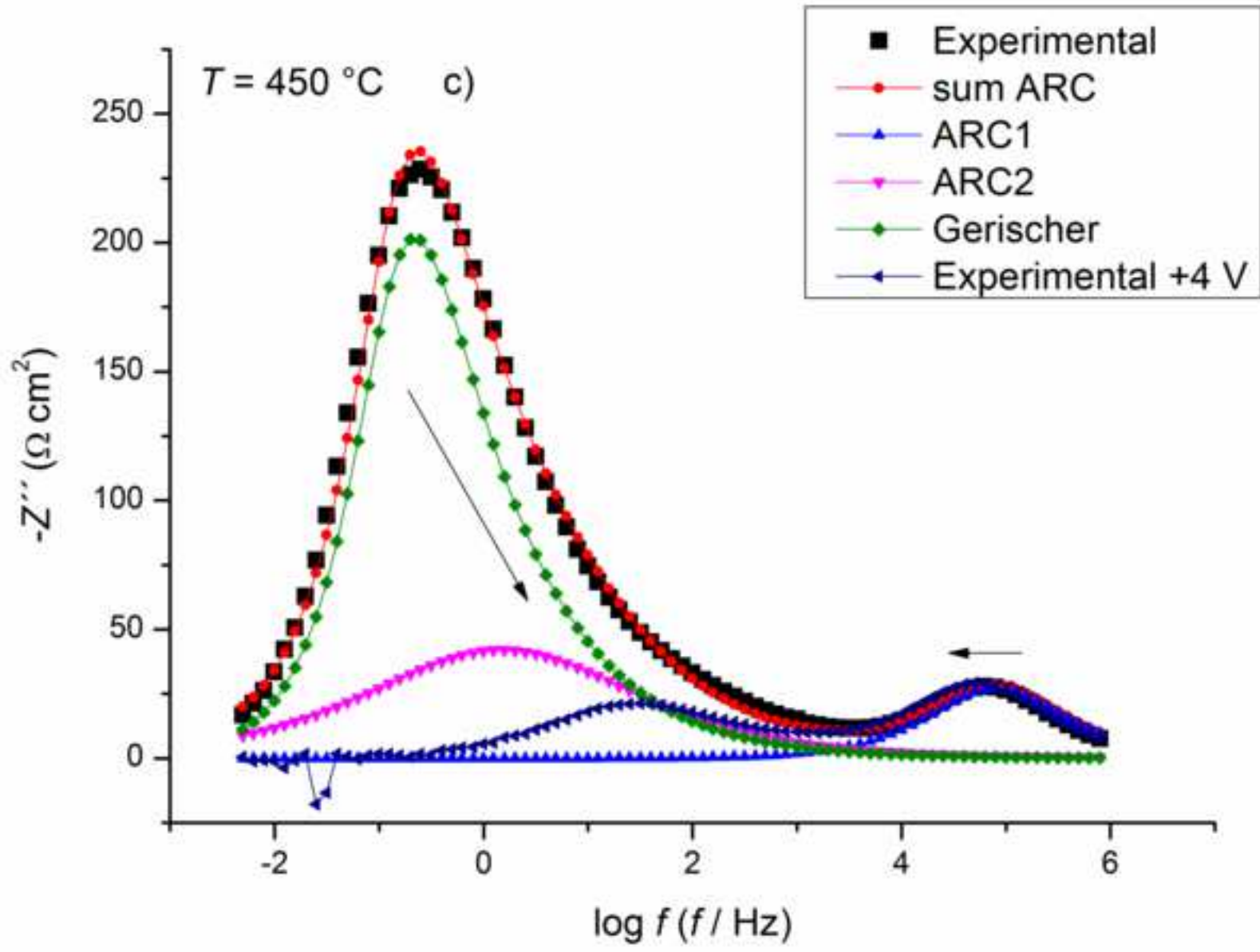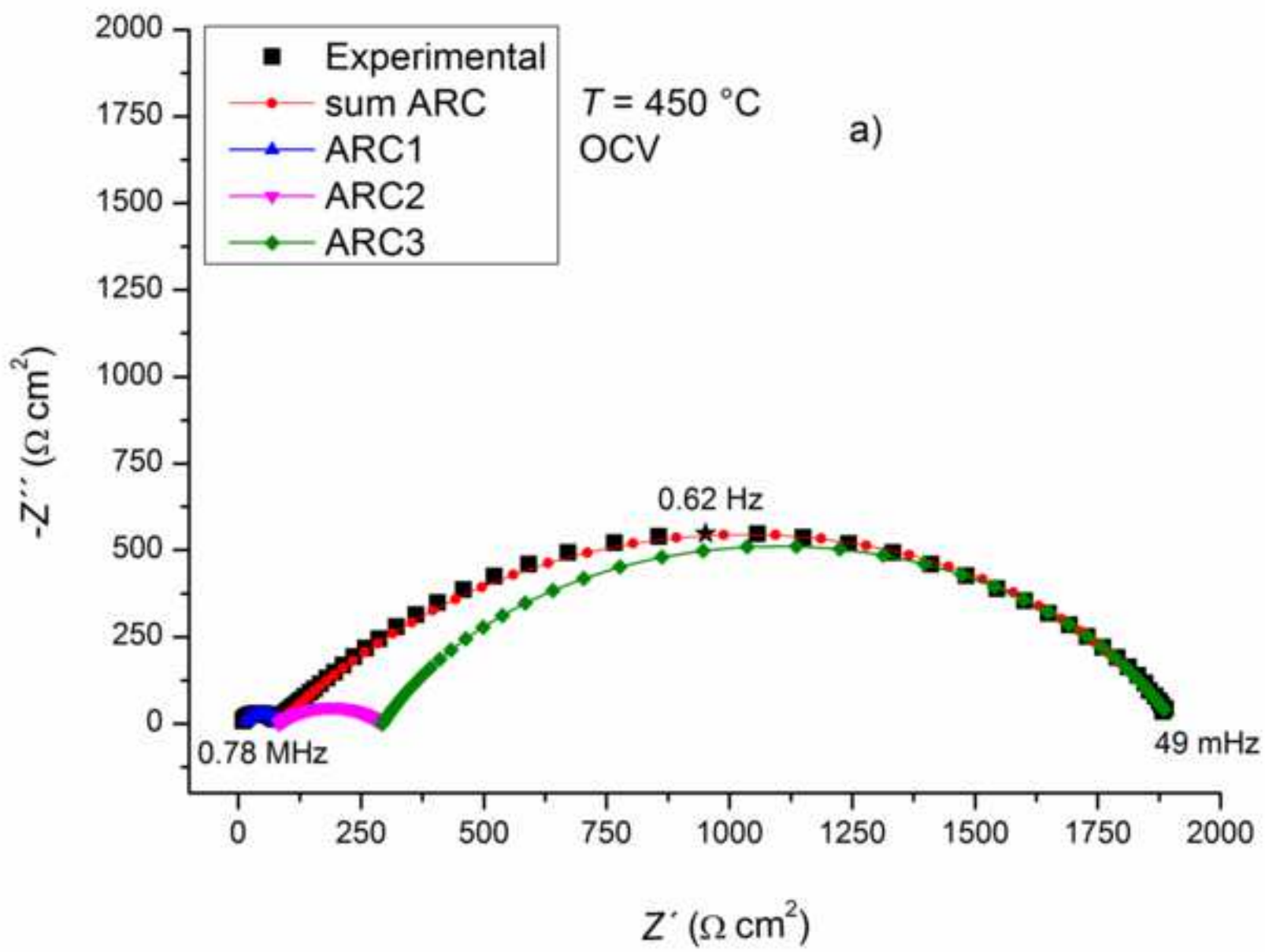
Figure 10a

Figure 11c

Figure 12

Figure 14
Click here to download high resolution image